BIOPHYSICS

The complex structure of *Fomes fomentarius* represents an architectural design for high-performance ultralightweight materials

Robert Pylkkänen[1,2]†, Daniel Werner[3]†, Ajit Bishoyi[4], Dominik Weil[5], Ernesto Scoppola[3], Wolfgang Wagermaier[3], Adil Safeer[4], Salima Bahri[4], Marc Baldus[4], Arja Paananen[1], Merja Penttilä[1,2], Géza R. Szilvay[1], Pezhman Mohammadi[1]*

High strength, hardness, and fracture toughness are mechanical properties that are not commonly associated with the fleshy body of a fungus. Here, we show with detailed structural, chemical, and mechanical characterization that *Fomes fomentarius* is an exception, and its architectural design is a source of inspiration for an emerging class of ultralightweight high-performance materials. Our findings reveal that *F. fomentarius* is a functionally graded material with three distinct layers that undergo multiscale hierarchical self-assembly. Mycelium is the primary component in all layers. However, in each layer, mycelium exhibits a very distinct microstructure with unique preferential orientation, aspect ratio, density, and branch length. We also show that an extracellular matrix acts as a reinforcing adhesive that differs in each layer in terms of quantity, polymeric content, and interconnectivity. These findings demonstrate how the synergistic interplay of the aforementioned features results in distinct mechanical properties for each layer.

INTRODUCTION

Many lightweight biological materials such as wood, bone, and silk exhibit exceptional strength, hardness, and fracture toughness that are crucial for their physiological functions (*1*–*6*). They are composed of hard and soft building blocks with characteristic dimensions ranging from nano- to mesoscales hierarchically arranged into a complex multiphase multicomponent composite. These properties are not commonly associated with the fleshy body of a fungus, yet the diversity of biological materials is extremely rich, and thus, it is perhaps expected that the multicellular fruiting bodies produced by fungi have great variance not only in terms of their appearance and edibility but also in their extraordinary material properties (*7*–*9*).

A particularly interesting species for advanced materials applications is the tinder fungus *Fomes fomentarius*, which produces lightweight polypore fruiting bodies that have been used for thousands of years as leathery and soft felt-like materials with excellent mechanical durability (*10*, *11*). *F. fomentarius* is a very common inhabitant of birch and beech forests all across the Northern Hemisphere, where it has an important biological function in releasing carbon and other nutrients that would otherwise remain sequestered by the dead trees (*12*). More specifically, the mycelium of *F. fomentarius* penetrates trees through damaged surfaces and grows inside them, decomposing cellulose, hemicellulose, and lignin in a process called white rot (*13*).

Outside trees, the only visible part of the fungus is the fruiting body, which has a primary biological function in the sexual propagation of the fungus via the discharge of basidium as basidiospores from the hymenium. In the case of *F. fomentarius*, the hymenium is arranged into porous structures called hymenophore tubes (H. tubes), which have an important role in increasing the available surface area for releasing a large number of spores from the hymenium (*14*). In terms of possible triggers for spore discharge, existing literature reports suggest that *F. fomentarius* sporulates at relatively low temperatures in spring and autumn and displays nocturnal patterns of spore discharge (*15*, *16*). Despite not being reported for *F. fomentarius*, it is worth noting that some fungal species have also been reported to discharge spores upon impact (*17*).

Unexpectedly, the fruiting bodies of *F. fomentarius* and their material properties have received the attention of the scientific community only very recently (*18*, *19*), despite having great potential for producing biodegradable leather-like materials from lignocellulosic biomass. Furthermore, to our knowledge, there are no widely accepted explanations for the specific mechanical roles of the different structural elements found in the fruiting bodies of bracket fungi, although they could serve as a source of inspiration for the production of multifunctional ultralightweight materials with properties that could potentially surpass natural materials in the future. However, perennial polypores typically produce hard and persistent fruiting bodies that have to be able to resist the different natural disturbances they encounter during their existence. For example, it is relatively easy to imagine impacts generated from falling objects, such as tree branches, or loads generated by climate conditions, such as wind and snow. The fruiting body should also have sufficient protection to resist attacks from fungivores such as beetles, yet it should be noted that some of these organisms may also help the fungus spread its spores more efficiently (*20*).

In this study, we report detailed structural, chemical, and mechanical characterization of the complex architectural design of *F.*

[1]VTT Technical Research Centre of Finland Ltd., Espoo, FI-02044 VTT, Finland. [2]Department of Bioproducts and Biosystems, School of Chemical Engineering, Aalto University, FI-00076 Aalto, Finland. [3]Department of Biomaterials, Max Planck Institute of Colloids and Interfaces, D-14476 Potsdam, Germany. [4]NMR Spectroscopy, Bijvoet Center for Biomolecular Research, Utrecht University, Padualaan 8, 3584 CH Utrecht, Netherlands. [5]KLA-Tencor GmbH, Moritzburger Weg 67, Dresden 01109, Germany.
*Corresponding author. Email: pezhman.mohammadi@vtt.fi
†These authors contributed equally to this work.

fomentarius fruiting bodies in terms of three distinct layers: crust, context, and H. tubes (Fig. 1). We further describe the distinct microstructure of mycelium in each layer with unique preferential orientation, aspect ratio, density, and branch length. We also report how the cell wall and extracellular matrix differ for each layer in terms of quantity, polymeric content, and interconnectivity. These results could offer a great source of inspiration for producing multifunctional materials with superior properties for diverse medical and industrial applications in the future (*10*, *21*–*23*).

RESULTS

Ultrastructure of *F. fomentarius*

On the microscale level, the effective component of this unique material is the fungal network of hyphae that form the mycelium. The hyphal cell wall, in turn, is composed of nanoscale structures formed by chemical interactions between molecules such as polysaccharides, proteins, lipids, pigments, and negligible quantities of inorganic components. At the general level, the development of *F. fomentarius* fruiting bodies is a multistep process of differentiation and multicellular growth. Changes initiate at the genomic level, which ultimately alters hyphal behavior and physiology in response to external stimuli, such as light, temperature, gravity, humidity, and/or molecular signals (*24*). The large fruiting bodies produced by *F. fomentarius* may reach a diameter of up to 50 cm and grow while the fungus decomposes the tree in a process that may span over 30 years. Typically, between one and three new hymenial layers are produced each year, from which the fungus can release up to 240 million spores/cm^2 per hour (*14*). Artificial indoor cultivations of *F. fomentarius* fruiting bodies have not yet been reported to our knowledge, and therefore, the exact mechanisms and signals that induce fruiting body formation in this species remain unclear.

To begin the characterization of the complex structure of *F. fomentarius* fruiting bodies, we started by dissecting a collected specimen into individual sections. Imaging of the cross section and surface of the fruiting body revealed that it consists of a multiscale hierarchical structure with three distinct macroscale layers, each varying in thickness and microstructural features (Figs. 1 and 2, A to C, and movies S1 to S6). The exterior region of the fruiting body consists of a hard and rigid protective outer layer known as the crust (Fig. 2A and movie S1). Using high-resolution x-ray microcomputed tomography (μCT) and scanning electron microscopy (SEM), we characterized the crust layer as a dense and uniform structure, with low porosity and no apparent microscale structural features. In addition, the mycelium network in this layer was heavily embedded and glued in an extracellular matrix. We also noted that the thickness of the crust is not uniform and characterized it as ranging from 900 μm at the posterior to 200 μm in the anterior region. Moreover, micrometer-sized cracks were observable with both SEM and μCT images at the surface of the crust, but these were dismissed as artifacts that likely emerged when the samples were prepared into thin slices.

Subjacent to the crust is the foam-like, soft, and leathery layer known as the context. We observed a gradual transition at the interface between the crust and context, with segments of the mycelium network being partially embedded in the same extracellular cement as in the crust. This gradient ultimately reaches a point where the mycelium can be seen free from any extracellular matrix in the context (Fig. 2B and movie S1), and the hyphae (diameter, ~2 μm) are partially aligned and oriented with branch lengths up to hundreds of micrometers.

The final layer subjacent to the context consists of hollow tubular structures known as H. tubes, which have preferential orientation and are arranged in parallel alignment with gravitational force (Fig. 2C and movies S2 to S4) (*14*). The walls of H. tubes consist

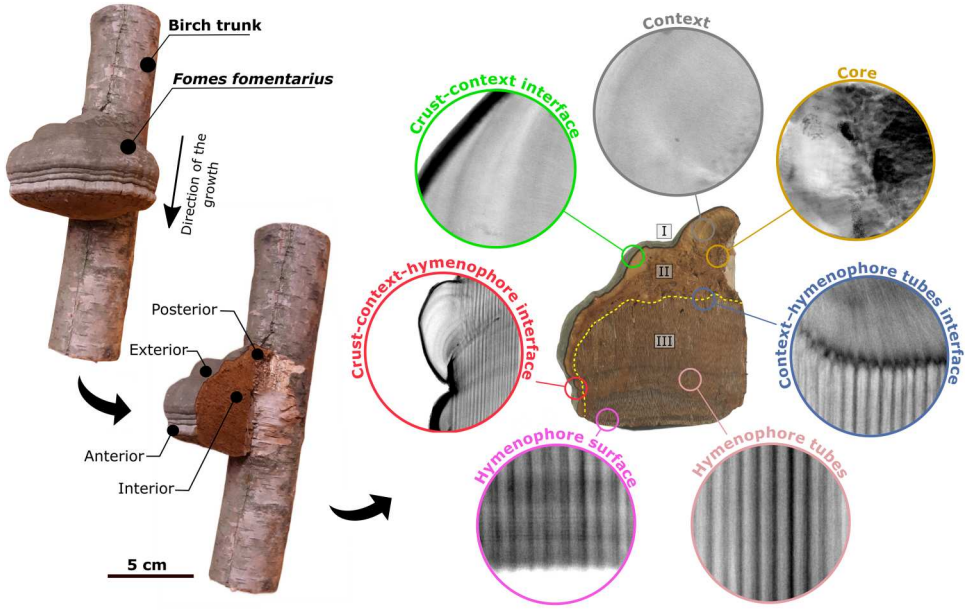

Fig. 1. The ultra-architecture of *F. fomentarius* used in this study. The x-ray 2D projections of the three main regions crust (I), context (II), and H. tubes (III) and their corresponding interfaces (circles) are shown. The imaginary yellow dashed line stretches from the posterior to the anterior region, indicating the boundary between the context and the H. tube layer.

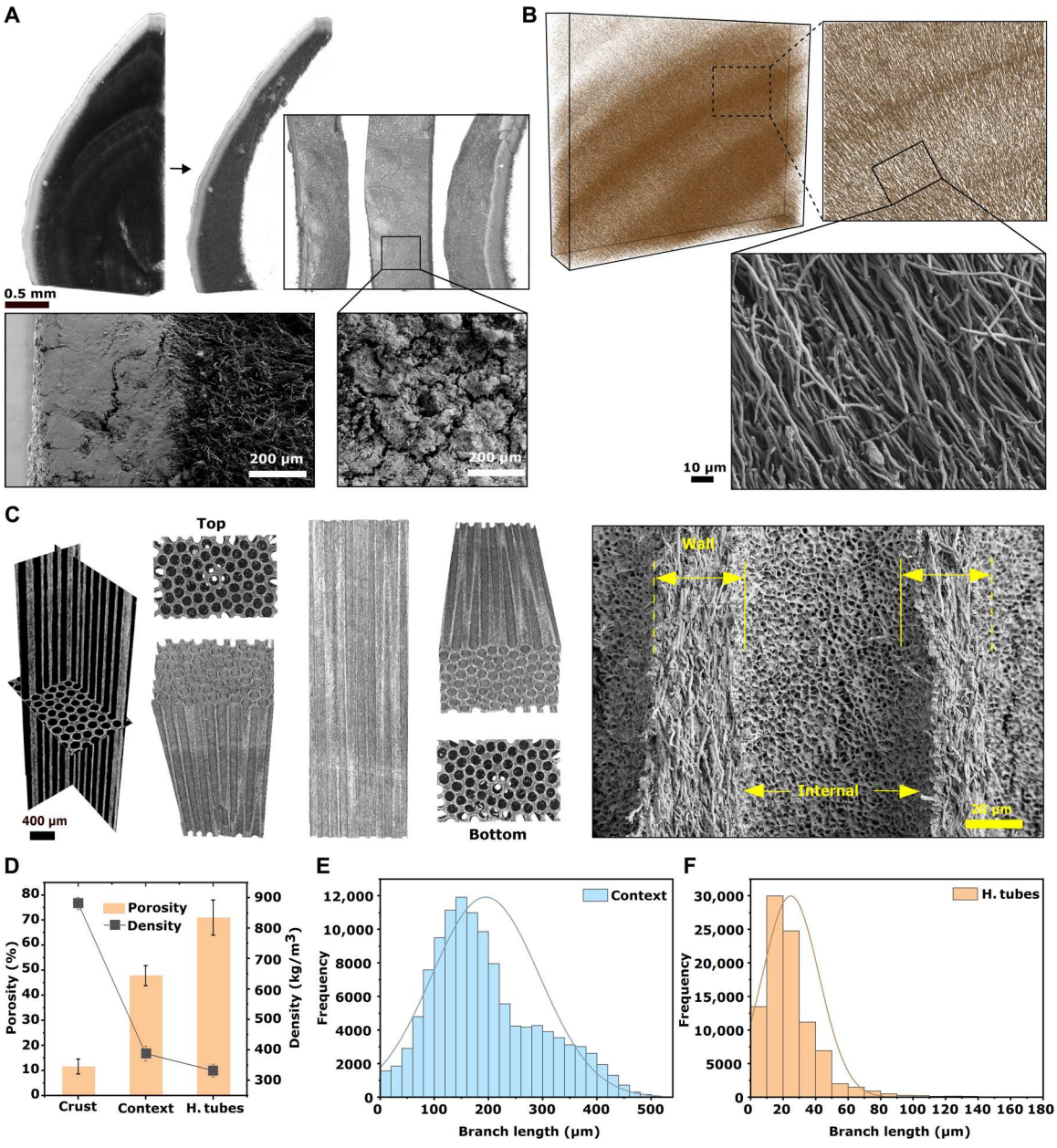

Fig. 2. A closer look at the three distinct main regions of the fruiting body using x-ray µCT and high-resolution SEM. (**A**) µCT and SEM images of the cross section and surface of the crust. (**B**) µCT and SEM image of the context. (**C**) *X-Y-Z* CT slices and 3D reconstruction of H. tubes at various rotating positions. (C) also demonstrates an SEM image of the cross section. The internal region and the tube walls are indicated by yellow dashed lines. (**D**) Calculated percentage porosity from µCT slides for all three regions. The plot also demonstrates the calculated density for each layer. (**E** and **F**) Calculated branch length of the hyphae in the context as well as the H. tubes.

of a shared mycelium network (thickness of about 20 to 50 µm) without clear boundaries between adjacent tubes, and the mycelium is preferably arranged in parallel orientation with the longitudinal axis of H. tubes. The mycelium network in the tubes is also glued by an extracellular matrix as in the crust but in substantially lower quantities.

The other prominent features that could be extracted from µCT and SEM images and differ in each layer are porosity and density. The quantified porosity and density for each layer were calculated to be approximately 11.5 ± 3, 47.7 ± 4, and 70.9 ± 7%, and 875 ± 23, 369 ± 57, and 337 ± 31 kg/m^3 for the crust, context, and H. tubes, respectively (Fig. 2D). In agreement with visual observations, these values confirm that the crust forms the densest and least porous layer, whereas the context and H. tubes form the least dense and most porous layers. Given that the mycelium network is the primary building block in all three layers, the main structural differences between the layers are dictated by the proportion of the network density, extracellular cement embedding the hyphae, and the notion that H. tubes contain a substantial hollow space.

As noted earlier, differences in branch length were also evident between hyphae in context and H. tubes, and therefore, we quantified branch lengths more thoroughly by analyzing μCT data (Fig. 2, E and F). The average branch length for hyphae in the context was about 200 μm, while in the H. tubes, the branch length was shorter at around 25 μm. With an apparent 10-fold difference in branch length, it would seem reasonable to suggest that the hyphae in context would prefer elongation over branching, while in H. tubes, they would prefer branching over elongation. It seems likely that the highly oriented tube walls are a result of frequent branching events that lead to a realignment of the hyphal growth direction. We could not quantify the branch length in the crust as the mycelium network could not be distinguished in the μCT slices. Last, in addition to these three main layers, other structural elements are also present in the fruiting bodies, such as a core structure that connects the fruiting body to the tree (Fig. 1 and movie S6) and cone-shaped transition points at the interfaces of the context and H. tubes that result in the emergence of H. tubes (Fig. 1 and movie S5).

H. tubes form the major portion of the fruiting body

Among all, the H. tubes were found to be the most prominent component of structural organization found in the fruiting body. Their contribution to the bulk of the fruiting bodies is about ~69%, whereas the crust and context contribute about ~4 and ~29%, respectively (Fig. 1). To gain a better understanding of the architecture of H. tubes, we reconstructed both the tube walls and their corresponding hollow space in 3D (Fig. 3A). These reconstructions highlight the extremely consistent alignment, orientation, spacing, size, and diameter of the tubes and the absence of skewed or otherwise misaligned/misoriented H. tubes.

Our next question was whether H. tubes are structurally consistent across their longitudinal axis. To examine this, we split the H. tubes across the longitudinal axis into five equally spaced zones and analyzed the consistency of H. tube architecture in each zone separately (Fig. 3B). We chose a naming scheme where zone I corresponds to the section of H. tubes at the top of the fruiting body, zone III corresponds to the middle, and zone V corresponds to the bottom. We did this to identify differences between the H. tubes located at the top (older regions) and the bottom (younger regions) of the fruiting body. Although the tubes can reach lengths up to 4 cm, there seems to be a consistent gradual change in their architecture between the different zones. The greatest deviations from the general tube architecture are found in zones I and II, which are situated closest to the interface region. Making a closer visual observation revealed elliptical cross sections as opposed to circular ones, and even fusions between two adjacent H. tubes are the origin of the larger variations. This is consistent with the notion that mycelium in the context differentiates into the H. tubes; therefore, the observed inconsistency in the shape and the diameter of the tubes in zones I and II are intermediate transition points before completely taking the circular shapes in zones II, IV, and V.

Intrigued by how effectively the hyphae network forming the mycelium is spatiotemporally controlled at the microscale length scale, we then turned our attention to examining the exact transition boundary between the context and H. tubes, above the tubular structures in zone I (Fig. 3C). To our surprise, we found that the mycelium (i) undergoes substantial preferential alignment in the context, (ii) merges into well-defined and equally spaced bundles of micrometer-sized cone-like assemblies (referred later to as "growth cones"), and (iii) subsequently produces an extracellular matrix that provides sufficient structural stability and rigidity for these unique constrained domains to initiate the formation of the H. tubes. Ultimately, well-defined tubular shapes with hollow spaces could be maintained by the shorter branch length and lower aspect ratio of the mycelium network (Fig. 2, E and F). Considering that the wall thickness between the two neighboring tubes is only about 20 to 50 μm, it is the most effective means of facilitating tight packing in such a confined space (Fig. 3A). We also noted growth cones that did not result in mature H. tubes, at an approximate 45° angle compared to the growth cones that resulted in mature H. tubes. Between these two sets of growth cones is a layer with an appearance that resembles the context. As bracket polypores typically exhibit gravimorphogenetic responses to produce new fruiting structures suitably reoriented to new spatial positions (*25*), these misaligned cones could be an indication of the different orientation of the birch trunk at some point during the lifetime of the fungal specimen.

Last, we looked into the open pores of H. tubes, located at the bottom of the fruiting body (corresponding to zone V) (Fig. 3C). As noted earlier, H. tubes in these zones had a generally similar appearance to zones III and IV, with the exception of a hollow spherical region centered around the empty space at the open end of each H. tube, as opposed to a flat opening. The primary mycelium, which can be found inside the walls of H. tubes, had a preferred parallel orientation to the tubes, while tertiary mycelium, which covers the surfaces of the walls and releases spores, tends to have a preferred orientation toward the center of the tubes (Fig. 3D).

Structural and chemical analysis

To better understand the nanoscale structural and chemical features found in the fruiting bodies of *F. fomentarius*, we next carried out various noninvasive spectral analyses of the three main layers. First, by using synchrotron wide- and small-angle x-ray scattering (WAXS/SAXS), we measured both profiles for a slice of the fruiting body that contained all three of the main layers and their corresponding interfaces (Fig. 4, A to C). The highest signal intensities could be obtained from the crust layer, followed by H. tubes and context, with peak intensities centered generally around the same q values. This trend has a direct correlation to the degree of crystallinity in each layer (fig. S1), with the crust showing the highest crystallinity index at 87 (±6)%. This is followed by a substantial decrease to 42 (±4)% for the context, and, once more, an increase to about 81 (±3)% for the H. tubes. The diffraction data, the SEM images, and the μCT slice (Fig. 4, A and B) all depict the high degree of crystallinity in the crust and the H. tubes directly associated with the embodiment of the mycelium network in a crystalized extracellular glue, in contrast to the context with no apparent extracellular matrix.

To estimate differences in the orientation of the mycelium network, we calculated Herman′s orientation parameter (HOP) from the azimuthal integration of 111 arc from the synchrotron WAXS measurements (Fig. 4A). This result revealed a gradual increase in orientation moving from the crust to the H. tubes. According to our calculations, orientation is the lowest in the crust layer (with an approximate HOP value of 0.0), increases slightly for the context (~0.25), and is the highest in H. tubes (~0.4). These

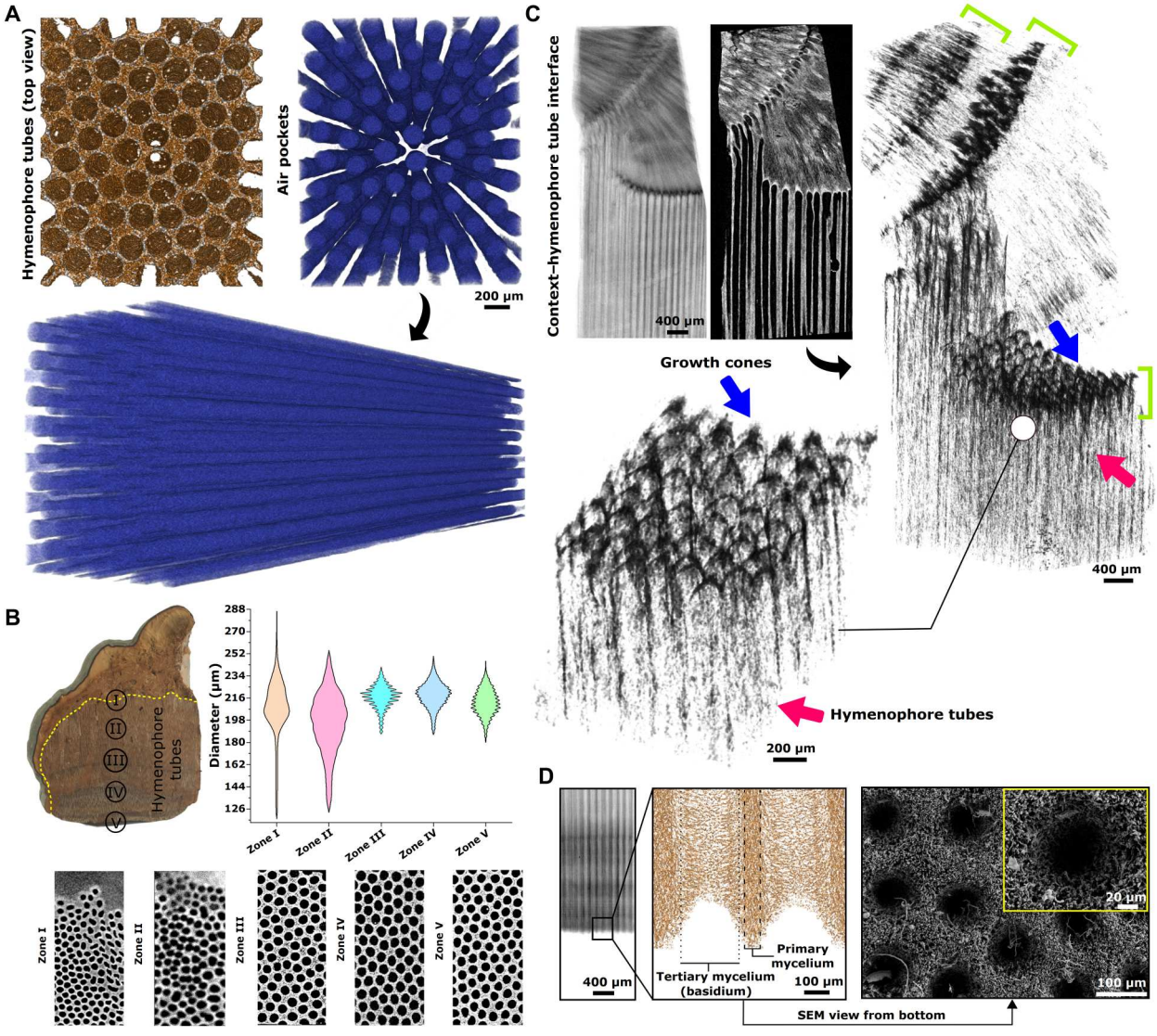

Fig. 3. Hymenophore tubes form the largest area in the *F. fomentarius*. (**A**) 3D reconstruction of H. tubes (golden brown) and the calculated empty space of each tube (blue). The air pockets are shown from the top and side views. (**B**) The calculated diameter of the H. tubes for five different zones and the representative µCT slices. (**C**) Interface between the context and H. tubes (corresponding to zone I) demonstrating preferential alignment of the mycelium network in the context region before assembling into growth cones, which ultimately templates the formation of the tubes (the individual cone indicated with the blue arrow, tube with the red arrow, and the array of the growth cone with the green square bracket). (**D**) A closer look at the H. tube's surface where the spores are released (most active region of the fruiting bodies), illustrating the primary and tertiary mycelium (corresponding to zone V).

observations were further confirmed and showed a similar trend by calculating orientation parameters from µCT data (fig. S2). This quantitative determination of orientation corresponds well with the qualitative observations provided by SEM images.

To better understand the composition of the molecular building blocks in each layer, we measured WAXS one-dimensional (1D) diffraction patterns for each layer (Fig. 4C). We found that the major peak profile for all the layers predominantly arises from triple-helical β-1,3-glucan, which has been shown to crystallize into supramolecular assemblies (*26*). While the x-ray profiles between the context and H. tubes seemed to be similar (major differences in the intensities), the crust layer showed an additional broad diffraction peak centered around 18.2 nm^{-1} and few other narrow peaks at 3.7, 6.6, and 7.4 nm^{-1}, which could not be assigned clearly on the basis of the literature. We expected these peaks to arise mostly from polysaccharides, proteins, lipids, pigments, or even inorganic salts, as these are the most commonly reported constituents for fruiting bodies of bracket fungi (*27*). Thus, we further examined the overall chemical composition of the crust, context, and H. tubes, using attenuated total reflectance–Fourier transform infrared spectroscopy (ATR-FTIR) (Fig. 4D). In agreement with observations from x-ray diffraction, similarities between the context and H. tubes were evident also in ATR-FTIR, while the crust layer was substantial different from the other two, particularly in terms of lipid and protein content (fig. S3). Polysaccharides (~45 to 60%) were found to be the

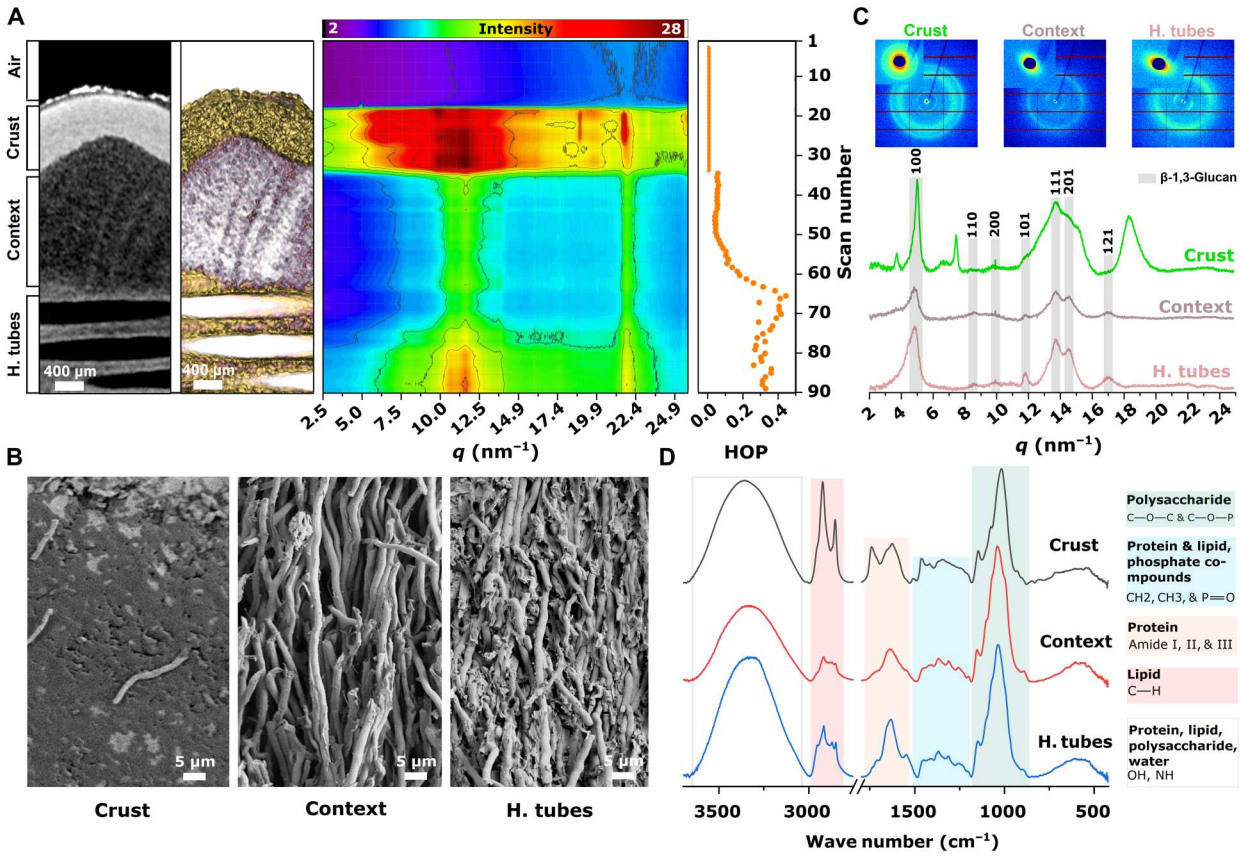

Fig. 4. The spectral analysis demonstrates distinct structural and chemical differences between the crust, context, and H. tubes. (**A**) *X-Y* CT slice of the crust–context–H. tube interface and the 3D reconstruction for the same region. (A) also demonstrates 92 simultaneous WAXS/SAXS measurements from the exterior to the interior side of the corresponding specimen. (A) also shows the calculated HOP by azimuthal integration of 111 arc as in (C). (**B**) High-resolution SEM imaging from each layer. (**C**) 1D and 2D WAXS/SAXS measurements corresponding to each layer. (**D**) ATR-FTIR measurement of the crust, context, and H. tubes corresponding to the layers imaged in (B).

dominating component, followed by protein (~20 to 30%) and waxes/lipids (~20 to 30%).

To elucidate further the composition of major polysaccharides and specific glycosidic linkages found in the three different layers, i.e., crust, context, and H. tubes, we used high-field magic angle spinning nuclear magnetic resonance (NMR) and measured proton-detected dipolar and scalar (*J*-based) ^{1}H-^{13}C correlation experiments (Fig. 5A) (*28*). This provided a means to study the rigid and mobile components of the fungal cell wall for natural abundance systems as previously assigned (*29*). As expected, β-glucan and chitin were found in all the layers. The first carbon chemical shift of α-glucan [C1, ~103.87 parts per million (ppm)] was found in the crust layer exclusively. Furthermore, a signal around 35 ppm (carbon) was only found in the crust layer, suggesting the presence of rigid proteins or/and lipids. We further estimated the relative abundance of each polysaccharide by peak integration analysis (Fig. 5B), as previously described for a ^{13}C-labeled fungal cell wall model (*30*). We estimated that the crust layer consists of 55% of both α-glucan and β-glucan, 1% of chitin, and 44% of other polysaccharides. The context layer consists of 69% of β-glucan, 2% of chitin, and 29% of other polysaccharides. Similarly, H.tubes layers consist of 38% of β-glucan, 5% of chitin, and 57% of other sugars. The other carbohydrates could refer to a combination of other major polysaccharides in the cell wall such as α-1,3-fucan, mannan, and β-1,6-glucan (*31*, *32*). Both the context and H-tubes showed identical chemical composition, with variation in relative occurrence. β-Glucan is more populated in the context layer, contributing more than 50% of the polysaccharides. In addition, we estimated the degree of deacetylation [DDA = (Int. Ch8/Int. Ch2) × 100; Ch8 and Ch2 stand for carbon atom 8 and 2 of chitin, respectively] amounting to 41 and 54% for the crust and H-tube layers, respectively. Unfortunately, this determination was not possible for the context layer because of insufficient signal-to-noise ratio. In addition, we recorded 2D scalar (*J*-based) ^{1}H-^{13}C heteronuclear correlation (hCH) experiments of all the layers to reveal the mobile components (polysaccharides/lipids/proteins). We observed mostly correlations that would be compatible with the mobile lipid acyl chain signals in all layers (assignments are given in fig. S4) (*33*).

In conclusion, the complexity of cell wall chemistry is depicted in Fig. 5C. We present a schematic of the approximate cell wall constituents that were measured for each layer using different spectral techniques in this section, as well as a general understanding of fungal cell wall architecture and chemistry, reported previously (*31*, *32*).

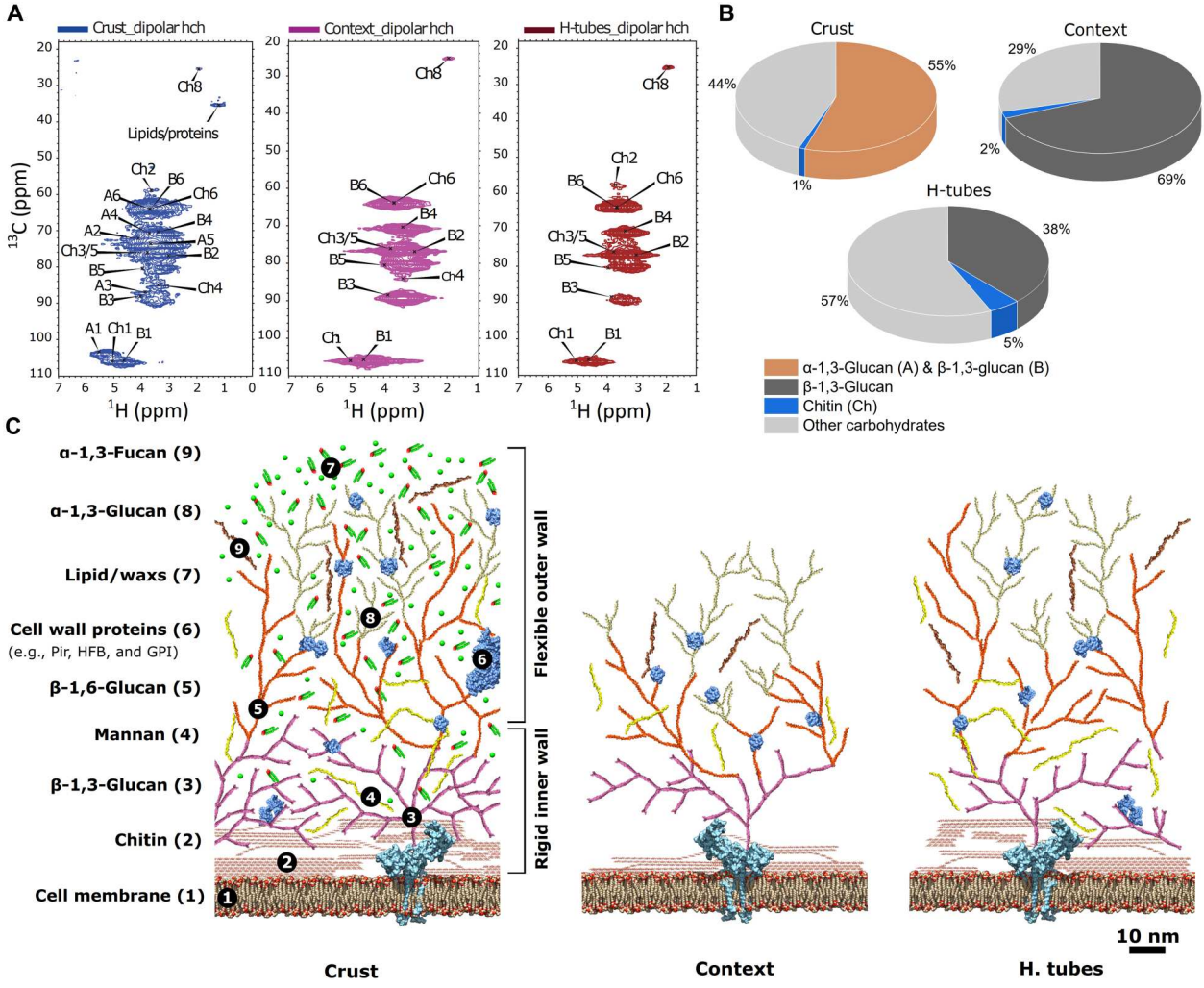

Fig. 5. Cell walls of the mycelium present in each layer exhibit distinct chemical composition and structural organization. (**A**) ^{1}H proton-detected [cross-polarization (CP)based] 2D ^{1}H-^{13}C correlation spectrum (with back CP of 200 μs) of the crust, context, and H-tubes. (**B**) Relative abundance of polysaccharides present in each layer calculated from the peak integration using Topspin. (**C**) Schematic representation of the mycelium's cell wall in the crust, context, and H. tubes. The major components, their interconnectivity, and their approximate position with respect to the cell membrane are shown.

Mechanical characteristics of the layers

Last, we correlated the obtained multiscale structural and chemical features of each layer to their mechanical properties. We systematically studied them by performing tensile, compression, and nanoindentation tests. Given that biological materials, in general, are highly responsive to humidity, we carried out the characterization at 50% relative humidity (RH) (*34*–*38*). As the first step, we performed tensile measurements, and Fig. 6A shows a typical stress-strain curve for the context and H. tubes. The tensile measurement for the crust could not be performed as it was prone to deformation and cracking during sample preparation because of the low thickness and inherent rigidity. For the H. tubes, the stress-strain response showed a yield curve with a positive slope until an instantaneous failure. However, the context showed a complicated shape, starting as a positive slope yield curve with an initial failure followed by a jagged trace and a secondary failure. The H. tubes showed ultimate strength, Young's modulus, and ultimate strain of 39.23 ± 11.7 MPa, 2.7 ± 0.7 GPa, and 2.8 ± 0.8%, respectively. For the context, the primary maximum strength, modulus, and strain were 5.8 ± 2.1 MPa, 0.3 ± 0.13 GPa, and 4.3 ± 2.6%, respectively, and the secondary stress and strain were 2.3 ± 0.84 MPa and 7.09 ± 5.1%, respectively. It is noteworthy to mention that the H. tubes exhibit Young's modulus and strength considering their density in comparison to various cellular materials such as softwood, hardwood, cork, leather, etc. (Fig. 6, B and C).

We then examined the fractured surfaces of both layers after the tensile tests using SEM to envision deformation and failure processes to verify the above strengthening and toughening mechanisms. Major differences between the two samples were identified (Fig. 6D). The H. tubes showed blunt surfaces that appeared to have smaller regions of the pullout. As evident from the finding described in the previous sections, this can be attributed to the synergistic interplay of a higher degree of network alignment, lower aspect ratio, and their embodiment in extracellular adhesive with a high degree of crystallinity (Fig. 4, A to C, and fig. S1), thus drastically increasing the interfacial area through covalent and

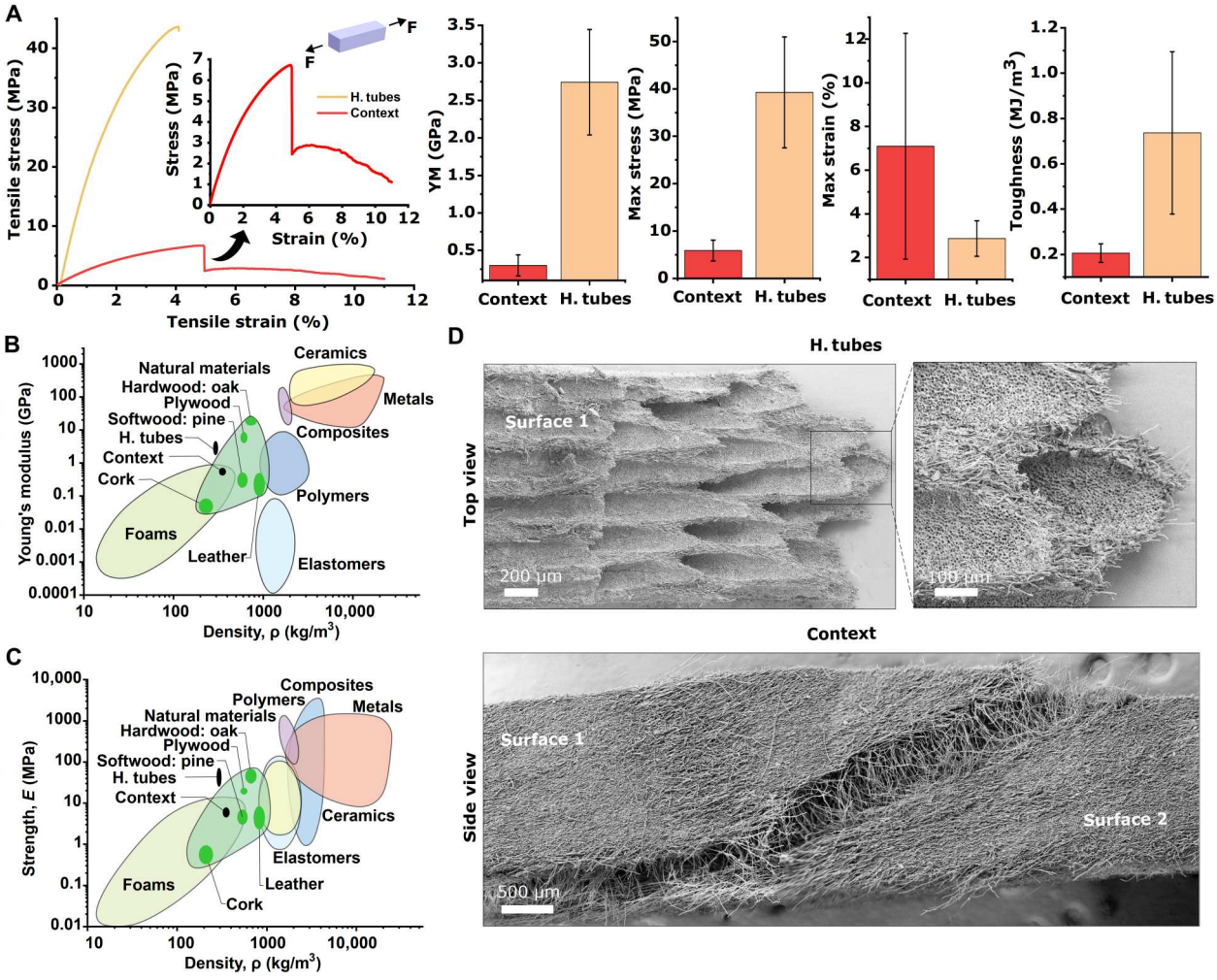

Fig. 6. Mechanical characterization of each layer. (**A**) Representative tensile stress-strain curves for the context and the H. tubes. Mean values ± SD (n = 8) for stress, strain, Young's modulus, and toughness are also shown. (**B** and **C**) Ashby plots comparing different types of natural and synthetic materials with the context and H. tube regions. Young's modulus versus density, as well as strength versus density. (**D**) SEM images were also taken from the fractured surfaces after tensile tests to better identify mechanical response and failure mechanisms.

noncovalent molecular interactions among hyphae microfibrils. Consequently, the mycelium network in the H. tubes can resist greater forces without undergoing major dislocations or substantial plastic deformations despite their high porosity and lower density but with the expense of lower tensile strain. However, the H. tubes show approximately 10-fold higher maximum strength and Young's modulus. This ultimately resulted in an overall greater modulus of toughness (area under the stress-strain curve) in the case of H. tubes (0.73 ± 0.3 MJ/m^3) versus context (0.2 ± 0.05 MJ/m^3).

In contrast, the mycelium network in the context exhibited segments of the mycelium network that remained connected to both interfaces even after the secondary failure. This directly correlates with the mechanical response and the observed two-stage failure mechanisms during tensile stress-strain measurements due to mycelium exhibiting a higher aspect ratio and lower interfacial adhesion (Fig. 6A). Under tensile load, the mycelium network in the context layer resists deformation until the forces surprise the elastic response of the interfacial matrix. This results in the context undergoing its primary failure, after which the mycelium experiences gradual sliding, energy dissipation, stretching hidden lengths, and unfolding of sacrificial bonds during the extension (jagged trace), until the final catastrophic failure. The plastic response for the extracellular matrix is well within the range of 2 to 4% strain, evident from the fracture response of both H. tubes and the primary failure point of the context (Fig. 6A).

To better associate the role of the network anisotropy and the interfacial matrix, we carried out compression tests on both the H. tubes and context either parallel or perpendicular to the orientation of the hyphae. For that, our specimens were prepared by cutting them either longitudinally or laterally in terms of observed macroscale architecture and the mycelium orientation. As expected, the results indicate that both layers have better compressive strength when the force of compression is parallel to the longitudinal axis of hyphae in the mycelium network, and furthermore, the greater orientation of H. tubes results in superior resistance to compressive forces at approximately 8 and 2 MPa, for longitudinal and lateral loading, respectively (Fig. 7A and movies S7 and S8), versus

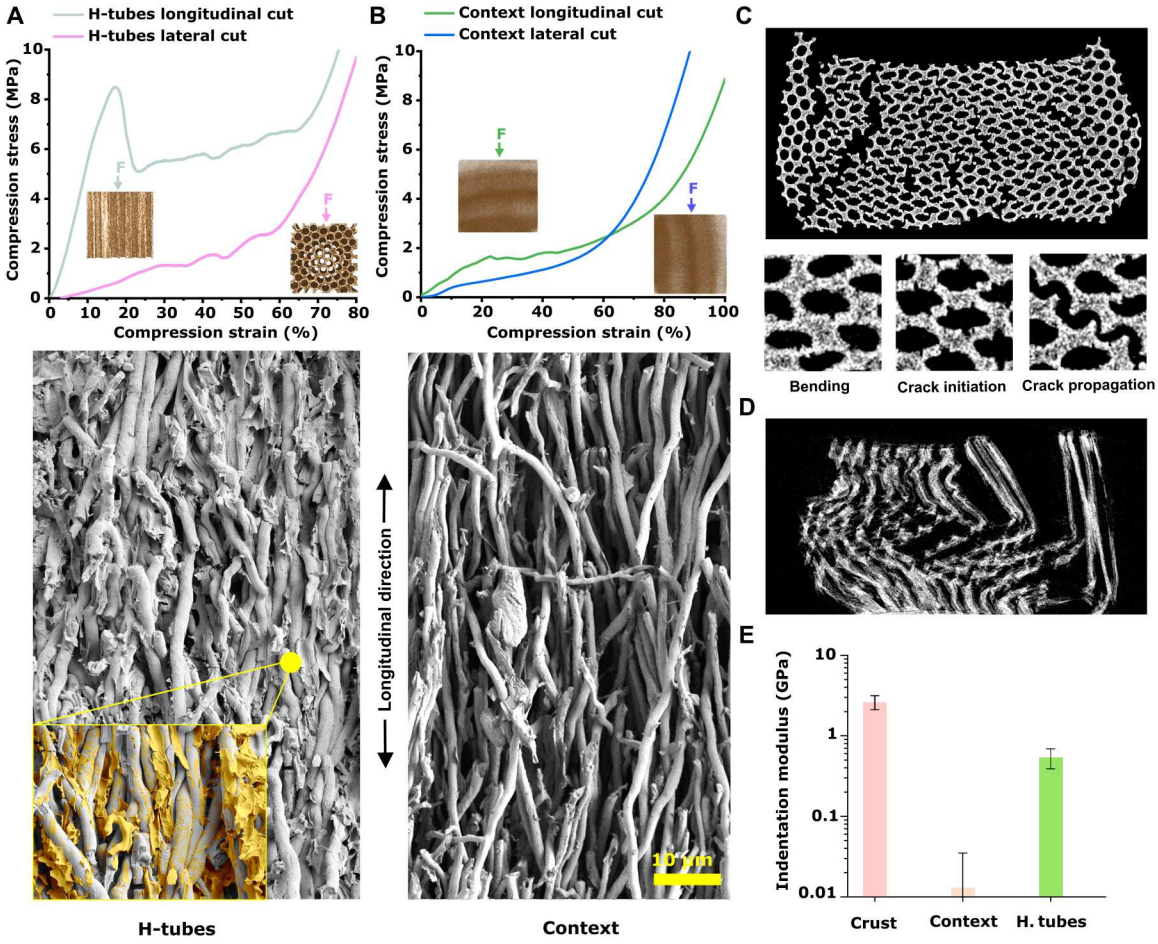

Fig. 7. The preferential orientation of mycelium in the longitudinal direction increased the mechanical performance of the materials. (**A** and **B**) Representative compression stress-strain curves for the context and H. tubes for specimens cut longitudinally and laterally. (A) and (B) also demonstrate high-resolution SEM images of the specimens before the compression test, illustrating the longitudinal orientation of the mycelium in the context and H. tubes. A falsely colored SEM image shows the presence of extracellular matrix that embedded and glued together the mycelium in the H. tube, whereas no extracellular matrix can be seen in the case of the context. (**C**) *X-Y* CT slice of the H. tubes after compression test showing that the material follows sequential energy dissipating failure. This includes bending, crack initiation, and, lastly, crack propagation for the lateral cut. (**D**) *X-Y* CT slice of the H. tubes cut longitudinally after compression test showing how the material dissipates energy through buckling effect. (**E**) Indentation modulus for the crust, context, and H. tubes.

compressive strength for the context at 1.8 and 0.61 MPa for longitudinal and lateral cuts, respectively (Fig. 7B and movie S9). In addition, the extracellular matrix in the H. tubes, which was absent in the context, is the major component for gluing together the mycelium network in H. tubes, thus improving the mechanical properties of H. tubes. To investigate the failure mechanisms during compression, we imaged both the laterally and longitudinally cut specimens after the measurements using µCT (Fig. 7, C and D). During transverse compression loading (Fig. 7C), sequential energy dissipating failure could be observed, where the walls of H. tubes bend until crack formation initiates, after which the cracks propagate along adjacent H. tubes. For parallel compression loading (Fig. 7D), H. tubes dissipate energy through the buckling effect, resulting in the malformation of H. tubes along the longitudinal axis.

Last, we measured the indentation modulus, i.e., for the crust, context, and H. tubes (Fig. 7E). These values were approximately 2.58 ± 0.48, 0.013 ± 0.02, and 0.53 ± 0.15 GPa for the crust, context, and H. tubes, respectively, evidencing that the crust, as the hard outer layer, has approximately 20- and 200-fold better resistance against wear and deformation in comparison to H. tubes and context, respectively.

DISCUSSION

F. fomentarius fruiting bodies are ingeniously lightweight biological designs, simple in composition but efficient in performance. They exhibit elegant strategies that fulfill not only a variety of mechanical needs, for example, protection (e.g., against insects or fallen branches/trees), but also functional needs that ensure propagation (spore formation and discharging), survival (unpreferred texture and taste for animals), and thriving of the multiyear fruiting body through the changing season. They are distinct from most biological materials as the living cells (hyphal cells) form the bulk part of the materials. What is found to be extraordinary is that, with minimal changes in their cell morphology and extracellular polymeric composition, they formulate diverse materials with distinct

physiochemical performances that surpass most natural and man-made materials that are usually confronted by property trade-offs (e.g., increasing weight/density to increase strength/stiffness/toughness).

We believe that the findings should attract a broad materials science audience and beyond (*10*, *22*, *23*, *39*). For researchers developing nanocomposites, our study provides a detailed characterization of biochemical principles to facilitate composite fabrication and enhance their mechanical properties (*40*–*42*). Given the outburst of interest in "living materials" in recent years (*43*, *44*), we envision that our approach will trigger other groups to explore *F. fomentarius*' promising fabrication routes for the next generation of programmable materials with high-performance functionalities capable of sensing, learning, self-repair, and adaptation (*45*–*48*). Production of materials from mycelium can be mediated by guiding the growth of the individual cell from the bottom up into almost any complexities and the desired functionalities with spatiotemporal control over their self-assemblies as explored extensively in other systems (*49*–*52*). Furthermore, growing the material using simple ingredients is an alternative solution to overcome the cost, time, mass production, and sustainability of how we make and consume materials in the future. The work should also attract the attention of polysaccharide engineers working on rationally designed carbohydrate-based materials produced through the use of synthetic biology and biotechnological processes (*53*). Last, the result should be appealing to biomaterial scientists and researchers from the biomedical industry, for example, in developing the next generation of 3D scaffolds for tissue engineering and orthopedic implants (*21*, *54*).

To our knowledge, artificial indoor cultivations have not been reported for *F. fomentarius* fruiting bodies. However, amadou produced from fruiting bodies of other bracket fungi, such as *Phellinus ellipsoideus*, has been reported to exhibit low tear resistance and tensile strength as well as high abrasion susceptibility (*55*). Studies related to the material properties of *F. fomentarius* have been carried out only recently in the form of laboratory-grown mycelium composite material (*18*). Depending on substrate and particle size, these mycelium composites have been reported to exhibit relatively weak mechanical performance in contrast to naturally occurring specimens, heretofore unexploited strategies from the natural design strategies. Typically, the laboratory-grown materials exhibit elastic modulus between 0.06 and 0.13 MPa and resisting compressive forces between 0.3 and 0.7 MPa (*18*). We believe that our comprehensive studies on the structure-chemical-property mechanisms could provide a source of inspiration for producing multifunctional mycelium-based materials in the future (*54*).

METHODS

General description of the used specimen

The *F. fomentarius* specimen was collected by harvesting a section of birch trunk containing the fruiting body of the fungal species (Vantaa, Finland). The general shape, size, and cross section of the fruiting body relative to the tree are shown in Fig. 1. More specifically, the dimensions of the fruiting body were measured to be 10 cm^3. The collected specimen was first dried using a lyophilizer, after which the sample preparations and storage were performed under ambient conditions. The fruiting body was dissected into individual sections representing each relevant layer, i.e., crust, context, H. tubes, and their interfaces.

Microcomputed tomography

Tomographic analysis was done with the high-resolution nanofocus computer tomography system X-Ray Micro CT EasyTom 160 (RX Solutions, Chavanod, France). This device contains a cesium iodide flat panel detector and two x-ray tubes, each with three different focal spot modes. The microtube is equipped with a tungsten filament and provides a maximum power of 150 kV and 500 μA. It can reach voxel sizes between 4 and 89 μm. The nanotube is equipped with a LaB6 filament and provides a maximum power of 100 kV and 200 μA. It can reach voxel sizes between 0.4 and 4 μm. All scans and reconstructions were carried out by using the software XAct from RX solutions. (i) Fifteen scans were performed with the microtube. For the CT scans with voxel sizes between 5 and 18 μm, the microtube with 80 kV + 80 μA = 6.4 W at the small focal spot mode was used. The source-detector distance was between 571.39 and 577.81 mm, and the source-object distance was between 22.48 and 81.91 mm. The frame rate of the flat panel detector was 3 with an average of five frames. By collecting 1120 images per turn, the scan time was 44 min after a calibration period of 20 min. (ii) Thirteen scans were performed with the nanotube. For the CT scans with voxel sizes between 1.50 and 4 μm, the nanotube with 80 kV + 68 μA = 5.4 W at the large and middle focal spot mode was used. The source-detector distance was between 626.05 and 738.47 mm, and the source-object distance was between 8.69 and 21.14 mm. The frame rate of the flat panel detector was 1 or 2 with an average of eight frames. By collecting 1120 images per turn, the scan time was 187 min (frame rate, 1) and 94 min (frame rate, 2) after a calibration period of 20 min.

Scanning transmission electron microscopy

SEM imaging was performed using a Zeiss FE-SEM field-emission microscope with variable pressure, operating at 1.5 kV, as previously reported (*34*, *35*, *38*). Shortly, all the specimens were sputtered with a 5- to 10-nm platinum-palladium layer before imaging. ImageJ Fiji (version 1.47d) software package was used for the visualization and analysis of the micrographs.

Synchrotron wide- and small-angle x-ray diffraction

WAXS/SAXS was carried out at the μSpot beamline at BESSY II (Berliner Elektronenspeicherring-Gesellschaft für Synchrotronstrahlung, Helmholtz-Zentrum Berlin, für Materialien und Energie, Germany). Measurements were performed with an energy exposure of 15 keV (0.82656 Å) using a silicon 111 monochromator and a beam size of 100 μm. Data were recorded using an Eiger X 9M detector with a pixel size of 75 μm × 75 μm, as reported previously (*56*, *57*). The measurements were carried out under ambient conditions at 50% RH. The specimens were clamped on a custom-made sample holder mounted on a motorized stage for positioning the samples perpendicular to the path of the beam. Diffractograms were recorded at 100 points along with the specimens (100 μm apart). Diffraction intensities around both the equator and meridian were integrated radially using the DPDAK software with a built-in algorithm from the pyFAI package, as reported previously (*35*). For all measurements, air scattering and dark current were subtracted from the diffractogram. Azimuthal intensity profiles at the (111) reflection were extracted by sector-wise integration after

masking the diffractogram to only reveal the (111) reflection ring. Subsequently, from the azimuthal intensity profile, the HOP was calculated according to Eqs. 1 and 2, and the orientation index was calculated according to Eq. 3. A combination of MATLAB and OriginLab was used for processing and visualizing the data

$$S = \frac{3}{2}\langle \cos^2\Phi \rangle - \frac{1}{2} \quad (1)$$

$$\langle \cos^2\Phi \rangle = \frac{\sum_0^{\pi} I(\Phi)\sin\Phi\cos^2\Phi}{\sum^{\pi} I(\Phi)\sin\Phi} \quad (2)$$

$$\Pi = \frac{180 - \mathrm{FWHM}}{180} \quad (3)$$

Attenuated total reflectance–Fourier transform infrared spectroscopy

The measurements were carried out using a Spectrum Two FTIR spectrometer (PerkinElmer) equipped with the diamond crystal. Unless otherwise stated, spectra were collected in the absorbance mode using 64 accumulative scans within the range of 400 to 4000 cm^{-1} and the resolution of 1 cm^{-1}.

Nuclear magnetic resonance

Each sample (i.e., crust, context, and H. tubes) was crushed and homogenized by mortar and pestle and then hydrated overnight in distilled water. All the samples were spun down at 150,000*g* to remove excess water and packed into separate 1.3-mm rotors for solid-state NMR measurements. All dipolar hCH proton-detected solid-state NMR experiments were measured at a magnetic field of 1.2 GHz (28.2 T). In addition, scalar-based hCH 2D experiments were recorded at 700 MHz (16.5 T). All samples were spun to 60 kHz at the magic angle (~54.74°) relative to the static field and cooled so that the sample is effective at room temperature, according to previous calibrations (*58*). We used Topspin 4.1 for processing spectra and integration analysis. The spectra were assigned using the NMRFAM Sparky software (*59*). Further details and experimental parameters are given in the Supplementary Materials (table S1).

Tensile test

Tensile tests were performed using a 5-kN tensile/compression module (Kammrath & Weiss GmbH, Germany) using either 100-N load cells with an elongation speed of 2 μm/s and a gauge length of 5 mm. For tensile tests, the H-tubes and the context were cut into 15-mm-long stripes, 2 mm wide. To prevent slippage during the measurement, the ends of the specimens were glued 5 mm from their ends between two pieces of abrasive sandpaper. The elongation and stress were calculated according to Eqs. 4 and 5, respectively. SEM images were used to measure the cross section of the specimens accurately. All the data processing was performed by using in-house MATLAB-written scripts to extract the mean values and SDs for Young's modulus, maximum strength, maximum strain, and toughness (n = 7). All the measurements were carried out under ambient conditions under 50% RH. All the samples were at least equilibrated at 50% RH 24 hours before the measurements

$$\varepsilon = \frac{\Delta L}{L_0} = \frac{L - L_0}{L_0} \quad (4)$$

$$\sigma = \frac{F_n}{A} \quad (5)$$

Compression test

Compression tests were carried out using a TA.XTExpressC Texture Analyzer stable microsystem equipped with a 100-N load cell on specimens with dimensions of about 5 m^3. Unless otherwise stated, measurements were performed with a flat-face cylindrical probe with a diameter of 5 mm and a deformation speed of 2.5 μm/s up to the point of catastrophic failure and densification. Recorded data were processed and analyzed using the combination of Exponent Connect software and OriginLab version 2021.

Nanoindentation test

The nanoindentation experiments were performed on an iMicro (KLA Corporation, Milpitas, CA) using a diamond flat punch tip with a diameter of 10 μm. Dynamic indentation was used to perform local dynamic mechanical analysis in the range between 10 and 200 Hz at seven distinct frequencies (10, 17, 28, 45, 74, 122, and 200 Hz). Before each frequency sweep, a pretest compression of 1 μm is used. This procedure is performed on the three different regions of the mushroom sample to analyze the resulting modulus.

Supplementary Materials

This PDF file includes:
Figs. S1 to S4
Table S1
Legends for movies S1 to S9

Other Supplementary Material for this manuscript includes the following:
Movies S1 to S9

View/request a protocol for this paper from *Bio-protocol*.

REFERENCES AND NOTES

1. Z. Liu, Z. Zhang, R. O. Ritchie, On the materials science of nature's arms race. *Adv. Mater.* **30**, 1705220 (2018).
2. U. G. K. Wegst, H. Bai, E. Saiz, A. P. Tomsia, R. O. Ritchie, Bioinspired structural materials. *Nat. Mater.* **14**, 23–36 (2015).
3. W. Huang, D. Restrepo, J. Jung, F. Y. Su, Z. Liu, R. O. Ritchie, J. McKittrick, P. Zavattieri, D. Kisailus, Multiscale toughening mechanisms in biological materials and bioinspired designs. *Adv. Mater.* **31**, 1901561 (2019).
4. S. E. Naleway, M. M. Porter, J. McKittrick, M. A. Meyers, Structural design elements in biological materials: Application to bioinspiration. *Adv. Mater.* **27**, 5455–5476 (2015).
5. S. Xiao, C. Chen, Q. Xia, Y. Liu, Y. Yao, Q. Chen, M. Hartsfield, A. Brozena, K. Tu, S. J. Eichhorn, Y. Yao, J. Li, W. Gan, S. Q. Shi, V. W. Yang, M. Io Ricco, J. Y. Zhu, I. Burgert, A. Luo, T. Li, L. Hu, Lightweight, strong, moldable wood via cell wall engineering as a sustainable structural material. *Science* **374**, 465–471 (2021).
6. P. Grönquist, D. Wood, M. M. Hassani, F. K. Wittel, A. Menges, M. Rüggeberg, Analysis of hygroscopic self-shaping wood at large scale for curved mass timber structures. *Sci. Adv.* **5**, eaax1311 (2019).
7. D. A. Wardle, B. D. Lindahl, Ecology. Disentangling global soil fungal diversity. *Science* **346**, 1052–1053 (2014).

8. L. Tedersoo, M. Bahram, S. Põlme, U. Kõljalg, N. S. Yorou, R. Wijesundera, L. V. Ruiz, A. M. Vasco-Palacios, P. Q. Thu, A. Suija, M. E. Smith, C. Sharp, E. Saluveer, A. Saitta, M. Rosas, T. Riit, D. Ratkowsky, K. Pritsch, K. Põldmaa, M. Piepenbring, C. Phosri, M. Peterson, K. Parts, K. Pärtel, E. Otsing, E. Nouhra, A. L. Njouonkou, R. H. Nilsson, L. N. Morgado, J. Mayor, T. W. May, L. Majuakim, D. J. Lodge, S. Lee, K. H. Larsson, P. Kohout, K. Hosaka, I. Hiiesalu, T. W. Henkel, H. Harend, L. D. Guo, A. Greslebin, G. Grelet, J. Geml, G. Gates, W. Dunstan, C. Dunk, R. Drenkhan, J. Dearnaley, A. de Kesel, T. Dang, X. Chen, F. Buegger, F. Q. Brearley, G. Bonito, S. Anslan, S. Abell, K. Abarenkov, Global diversity and geography of soil fungi. *Science* **346**, 1256688 (2014).
9. G. R. Smith, B. S. Steidinger, T. D. Bruns, K. G. Peay, Competition-colonization tradeoffs structure fungal diversity. *ISME J.* **12**, 1758–1767 (2018).
10. A. Gandia, J. G. van den Brandhof, F. V. W. Appels, M. P. Jones, Flexible fungal materials: Shaping the future. *Trends Biotechnol.* **39**, 1321–1331 (2021).
11. N. Papp, R. Kinga, B. Tímea, D. Czégény, Ethnomycological use of *Fomes fomentarius* (L.) Fr. and *Piptoporus betulinus* (Bull.) P. Karst. in Transylvania, Romania. *Genet. Resour. Crop. Evol.* **64**, 101–111 (2017).
12. J. Judova, K. Dubikova, S. Gaperova, J. Gaper, P. Pristas, The occurrence and rapid discrimination of *Fomes fomentarius* genotypes by ITS-RFLP analysis. *Fungal Biol.* **116**, 155–160 (2012).
13. T. Větrovský, J. Voříšková, J. Šnajdr, J. Gabriel, P. Baldrian, Ecology of coarse wood decomposition by the saprotrophic fungus *Fomes fomentarius*. *Biodegradation* **22**, 709–718 (2011).
14. O. Schmidt, *Wood and Tree Fungi: Biology, Damage, Protection, and Use* (Springer-Verlag Berlin Heidelberg, 2006).
15. T. R. Rockett, C. L. Kramer, Periodicity and total spore production by lignicolous basidiomycetes. *Mycologia* **66**, 817–829 (1974).
16. F. W. M. R. Schwarze, J. Engels, C. Mattheck, Examination, importance and mechanical effects of wood-decay fungi in the living tree, in *Fungal Strategies of Wood Decay in Trees* (Springer Berlin Heidelberg, 2000), pp. 33–138.
17. M. O. Hassett, M. W. F. Fischer, N. P. Money, Mushrooms as rainmakers: How spores act as nuclei for raindrops. *PLOS ONE* **10**, e0140407 (2015).
18. C. Pohl, B. Schmidt, T. Nunez Guitar, S. Klemm, H.-J. Gusovius, S. Platzk, H. Kruggel-Emden, A. Klunker, C. Völlmecke, C. Fleck, V. Meyer, Establishment of the basidiomycete *Fomes fomentarius* for the production of composite materials. *Fungal Biol. Biotechnol.* **9**, 4 (2022).
19. C. Müller, S. Klemm, C. Fleck, Bracket fungi, natural lightweight construction materials: Hierarchical microstructure and compressive behavior of *Fomes fomentarius* fruit bodies. *Appl. Phys. A* **127**, 178 (2021).
20. D. S. Schigel, Polypore-beetle associations in Finland. *Ann. Zool. Fennici.* **48**, 319–348 (2011).
21. M. E. Antinori, M. Contardi, G. Suarato, A. Armirotti, R. Bertorelli, G. Mancini, D. Debellis, A. Athanassiou, Advanced mycelium materials as potential self-growing biomedical scaffolds. *Sci. Rep.* **11**, 12630 (2021).
22. H. Rischer, G. R. Szilvay, K.-M. Oksman-Caldentey, Cellular agriculture—Industrial biotechnology for food and materials. *Curr. Opin. Biotechnol.* **61**, 128–134 (2020).
23. S. Vandelook, E. Elsacker, A. van Wylick, L. de Laet, E. Peeters, Current state and future prospects of pure mycelium materials. *Fungal Biol. Biotechnol.* **8**, 20 (2021).
24. D. Moore, A. C. Gange, E. G. Gange, L. Boddy, Chapter 5 Fruit Bodies: Their production and development in relation to environment, in *British Mycological Society Symposia Series*, L. Boddy, J. C. Frankland, P. van West, Eds. (Academic Press, 2008), vol. 28, pp. 79–103.
25. D. Moore, Perception and response to gravity in higher fungi—A critical appraisal. *New Phytol.* **117**, 3–23 (1991).
26. Y. Deslandes, R. H. Marchessault, A. Sarko, Triple-helical structure of (1→3)-β-D-glucan. *Macromolecules* **13**, 1466–1471 (1980).
27. N. A. R. Gow, J.-P. Latge, C. A. Munro, The fungal cell wall: Structure, biosynthesis, and function. *Microbiol. Spectr.* **5**, 10.1128/microbiolspec.FUNK-0035-2016 (2017).
28. E. Barbet-Massin, A. J. Pell, J. S. Retel, L. B. Andreas, K. Jaudzems, W. T. Franks, A. J. Nieuwkoop, M. Hiller, V. Higman, P. Guerry, A. Bertarello, M. J. Knight, M. Felletti, T. le Marchand, S. Kotelovica, I. Akopjana, K. Tars, M. Stoppini, V. Bellotti, M. Bolognesi, S. Ricagno, J. J. Chou, R. G. Griffin, H. Oschkinat, A. Lesage, L. Emsley, T. Herrmann, G. Pintacuda, Rapid proton-detected NMR assignment for proteins with fast magic angle spinning. *J. Am. Chem. Soc.* **136**, 12489–12497 (2014).
29. H. L. Ehren, F. V. W. Appels, K. Houben, M. A. M. Renault, H. A. B. Wösten, M. Baldus, Characterization of the cell wall of a mushroom forming fungus at atomic resolution using solid-state NMR spectroscopy. *Cell Surface* **6**, 100046 (2020).
30. A. Safeer, F. Kleijburg, S. Bahri, D. Beriashvili, E. J. A. Veldhuizen, J. van Neer, M. Tegelaar, H. de Cock, H. A. B. Wösten, M. Baldus, Probing cell-surface interactions in fungal cell walls by high-resolution ^{1}H-detected solid-state NMR spectroscopy. *Chem. A. Euro. J.* **29**, e202202616 (2023).
31. I. Geoghegan, G. Steinberg, S. Gurr, The role of the fungal cell wall in the infection of plants. *Trends Microbiol.* **25**, 957–967 (2017).
32. X. Kang, A. Kirui, A. Muszyński, M. C. D. Widanage, A. Chen, P. Azadi, P. Wang, F. Mentink-Vigier, T. Wang, Molecular architecture of fungal cell walls revealed by solid-state NMR. *Nat. Commun.* **9**, 2747 (2018).
33. A. Pozza, F. Giraud, Q. Cece, M. Casiraghi, E. Point, M. Damian, C. le Bon, K. Moncoq, J. L. Banères, E. Lescop, L. J. Catoire, Exploration of the dynamic interplay between lipids and membrane proteins by hydrostatic pressure. *Nat. Commun.* **13**, 1780 (2022).
34. P. Mohammadi, M. S. Toivonen, O. Ikkala, W. Wagermaier, M. B. Linder, Aligning cellulose nanofibril dispersions for tougher fibers. *Sci. Rep.* **7**, 11860 (2017).
35. P. Mohammadi, J.-A. Gandier, N. Nonappa, W. Wagermaier, A. Miserez, M. Penttilä, Bioinspired functionally graded composite assembled using cellulose nanocrystals and genetically engineered proteins with controlled biomineralization. *Adv. Mater.* **33**, 2102658 (2021).
36. V. Hynninen, P. Mohammadi, W. Wagermaier, S. Hietala, M. B. Linder, O. Ikkala, Methyl cellulose/cellulose nanocrystal nanocomposite fibers with high ductility. *Eur. Polym. J.* **112**, 334–345 (2019).
37. A. Kamada, A. Levin, Z. Toprakcioglu, Y. Shen, V. Lutz-Bueno, K. N. Baumann, P. Mohammadi, M. B. Linder, R. Mezzenga, T. P. J. Knowles, Modulating the mechanical performance of macroscale fibers through shear-induced alignment and assembly of protein nanofibrils. *Small* **16**, 1904190 (2019).
38. P. Mohammadi, A. Sesilja Aranko, C. P. Landowski, O. Ikkala, K. Jaudzems, W. Wagermaier, M. B. Linder, Biomimetic composites with enhanced toughening using silk-inspired triblock proteins and aligned nanocellulose reinforcements. *Sci. Adv.* **5**, eaaw2541 (2019).
39. X. Y. Chan, N. Saeidi, A. Javadian, D. E. Hebel, M. Gupta, Mechanical properties of dense mycelium-bound composites under accelerated tropical weathering conditions. *Sci. Rep.* **11**, 22112 (2021).
40. M. Haneef, L. Ceseracciu, C. Canale, I. S. Bayer, J. A. Heredia-Guerrero, A. Athanassiou, Advanced materials from fungal mycelium: Fabrication and tuning of physical properties. *Sci. Rep.* **7**, 41292 (2017).
41. A. McGarry, K. S. Burton, Mechanical properties of the mushroom, *Agaricus bisporus*. *Mycol. Res.* **98**, 241–245 (1994).
42. D. L. Porter, S. E. Naleway, Hyphal systems and their effect on the mechanical properties of fungal sporocarps. *Acta Biomater.* **145**, 272–282 (2022).
43. X. Liu, H. Yuk, S. Lin, G. A. Parada, T. Tang, E. Tham, C. de la Fuente-Nunez, T. K. Lu, X. Zhao, 3D printing of living responsive materials and devices. *Adv. Mater.* **30**, 1704821 (2018).
44. C. Gilbert, T. C. Tang, W. Ott, B. A. Dorr, W. M. Shaw, G. L. Sun, T. K. Lu, T. Ellis, Living materials with programmable functionalities grown from engineered microbial co-cultures. *Nat. Mater.* **20**, 691–700 (2021).
45. L. K. Rivera-Tarazona, V. D. Bhat, H. Kim, Z. T. Campbell, T. H. Ware, *Shape-morphing living composites*, *Sci. Adv.* **6**, 10.1126/sciadv.aax8582 (2020).
46. P. Gordiichuk, S. Coleman, G. Zhang, M. Kuehne, T. T. S. Lew, M. Park, J. Cui, A. M. Brooks, K. Hudson, A. M. Graziano, D. J. M. Marshall, Z. Karsan, S. Kennedy, M. S. Strano, Augmenting the living plant mesophyll into a photonic capacitor. *Sci. Adv.* **7**, eabe9733 (2021).
47. F. Fu, L. Shang, Z. Chen, Y. Yu, Y. Zhao, Bioinspired living structural color hydrogels. *Sci. Robot.* **3**, 10.1126/scirobotics.aar85 (2018).
48. T. C. Tang, B. An, Y. Huang, S. Vasikaran, Y. Wang, X. Jiang, T. K. Lu, C. Zhong, Materials design by synthetic biology. *Nat. Rev. Mater.* **6**, 332–350 (2021).
49. X. Liu, M. E. Inda, Y. Lai, T. K. Lu, X. Zhao, Engineered living hydrogels. *Adv. Mater.* **34**, 2201326 (2022).
50. C. M. Heveran, S. L. Williams, J. Qiu, J. Artier, M. H. Hubler, S. M. Cook, J. C. Cameron, W. v. Srubar, Biomineralization and successive regeneration of engineered living building materials. *Matter* **2**, 481–494 (2020).
51. Z. Wang, H. Bai, W. Yu, Z. Gao, W. Chen, Z. Yang, C. Zhu, Y. Huang, F. Lv, S. Wang, Flexible bioelectronic device fabricated by conductive polymer-based living material. *Sci. Adv.* **8**, eabo1458 (2022).
52. M. Schaffner, P. A. Rühs, F. Coulter, S. Kilcher, A. R. Studart, 3D printing of bacteria into functional complex materials. *Sci. Adv.* **3**, eaao6804 (2017).
53. R. Pylkkänen, P. Mohammadi, V. Liljeström, W. Płaziński, G. Beaune, J. V. I. Timonen, M. Penttilä, β-1,3-Glucan synthesis, novel supramolecular self-assembly, characterization and application. *Nanoscale* **14**, 15533–15541 (2022).
54. S. Gantenbein, E. Colucci, J. Käch, E. Trachsel, F. B. Coulter, P. A. Rühs, K. Masania, A. R. Studart, Three-dimensional printing of mycelium hydrogels into living complex materials. *Nat. Mater.* **22**, 128–134 (2023).
55. J. Bustillos, A. Loganathan, R. Agrawal, B. A. Gonzalez, M. G. Perez, S. Ramaswamy, B. Boesl, A. Agarwal, Uncovering the mechanical, thermal, and chemical characteristics of biodegradable mushroom leather with intrinsic antifungal and antibacterial properties. *ACS Appl. Bio. Mater.* **3**, 3145–3156 (2020).

56. P. Mohammadi, F. Zemke, W. Wagermaier, M. B. Linder, Interfacial crystallization and supramolecular self-assembly of spider silk inspired protein at the water-air interface. *Materials* **14**, 4239 (2021).
57. P. Mohammadi, A. S. Aranko, L. Lemetti, Z. Cenev, Q. Zhou, S. Virtanen, C. P. Landowski, M. Penttilä, W. J. Fischer, W. Wagermaier, M. B. Linder, Phase transitions as intermediate steps in the formation of molecularly engineered protein fibers. *Commun. Biol.* **1**, 86 (2018).
58. K. R. Thurber, R. Tycko, Measurement of sample temperatures under magic-angle spinning from the chemical shift and spin-lattice relaxation rate of 79Br in KBr powder. *J. Magn. Reson.* **196**, 84–87 (2009).
59. W. Lee, M. Tonelli, J. L. Markley, NMRFAM-SPARKY: Enhanced software for biomolecular NMR spectroscopy. *Bioinformatics* **31**, 1325–1327 (2015).

Acknowledgments: We thank C. Li from the Max Planck Institute of Colloids and Interfaces in Potsdam, Germany, for help during synchrotron measurements at the μSpot beamline at BESSY at the Helmholtz-Zentrum Berlin für Materialien und Energie in Berlin, Germany. We acknowledge the provision of facilities and technical support by Aalto University at the OtaNano Nanomicroscopy Center (Aalto-NMC). **Funding:** This work was supported by the Academy of Finland project 348628, the Jenny and Antti Wihuri Foundation (Centre for Young Synbio Scientists), and the Academy of Finland Center of Excellence Program (2022–2029) in Life-Inspired Hybrid Materials (LIBER) project number 346106, and by internal funding from the VTT Technical Research Center of Finland Ltd. We also acknowledge the Dutch Research Council (NWO, domain Applied and Engineering Sciences: MYCOAT project number 18425) and the Horizon 2020 programs of the European Union (FUNGAR; project 58132 and iNEXT-Discovery, project 871037) for NMR studies. Furthermore, the high-field NMR experiments were supported by uNMR-NL, the National Roadmap Large-Scale NMR Facility of the Netherlands (NWO grant 184.032.207), and the uNMR-NL grid (NWO grant 184.035.002). **Author contributions:** Conceptualization: P.M., G.R.S., M.P., and A.P. Methodology: P.M., R.P., D.Wer., A.B., D.Wei., E.S., W.W., A.S., S.B., and M.B. Investigation: P.M., R.P., D.Wer., A.B., D.Wei., E.S., W.W., A.S., S.B., and M.B. Supervision: P.M. Writing—original draft: P.M. and R.P. Writing—review and editing: P.M., R.P., D.Wer., A.B., D.Wei., E.S., W.W., A.S., S.B., M.B., G.R.S., M.P., and A.P. **Competing interests:** The authors declare that they have no competing interests. **Data and materials availability:** All data needed to evaluate the conclusions in the paper are present in the paper and/or the Supplementary Materials.

Submitted 25 August 2022
Accepted 20 January 2023
Published 22 February 2023
10.1126/sciadv.ade5417